Nocturnal Low-Level Jet in a Mountain Basin Complex. Part I: Evolution and Effects on Local Flows

ROBERT M. BANTA AND LISA S. DARBY

NOAA/Environmental Technology Laboratory, Boulder, Colorado

JEROME D. FAST

Pacific Northwest National Laboratory, Richland, Washington

JAMES O. PINTO

National Center for Atmospheric Research, Boulder, Colorado

C. DAVID WHITEMAN AND WILLIAM J. SHAW

Pacific Northwest National Laboratory, Richland, Washington

BRAD W. ORR

NOAA/Environmental Technology Laboratory, Boulder, Colorado

(Manuscript received 25 November 2003, in final form 23 April 2004)

ABSTRACT

A Doppler lidar deployed to the center of the Great Salt Lake (GSL) basin during the Vertical Transport and Mixing (VTMX) field campaign in October 2000 found a diurnal cycle of the along-basin winds with northerly up-basin flow during the day and a southerly down-basin low-level jet at night. The emphasis of VTMX was on stable atmospheric processes in the cold-air pool that formed in the basin at night. During the night the jet was fully formed as it entered the GSL basin from the south. Thus, it was a feature of the complex string of basins draining toward the Great Salt Lake, which included at least the Utah Lake basin to the south. The timing of the evening reversal to down-basin flow was sensitive to the larger-scale north–south pressure gradient imposed on the basin complex. On nights when the pressure gradient was not too strong, local drainage flow (slope flows and canyon outflow) was well developed along the Wasatch Range to the east and coexisted with the basin jet. The coexistence of these two types of flow generated localized regions of convergence and divergence, in which regions of vertical motion and transport were focused. Mesoscale numerical simulations captured these features and indicated that updrafts on the order of 5 cm s^{-1} could persist in these localized convergence zones, contributing to vertical displacement of air masses within the basin cold pool.

1. Introduction

Many populated areas are located in intermountain basins, and basins are also sites of human-related activities, such as logging, mining, agriculture, water management, recreation, and industrial operations, among many others. Processes controlling transport and dispersion of atmospheric contaminants in basins are important to air quality, emergency response, fire weather, aviation, agriculture, and other applications. One such populated basin is the Great Salt Lake (GSL) basin, one of a complex of basins in central Utah. This basin was the site of the Vertical Transport and Mixing (VTMX) field campaign in October of 2000, which was designed to study meteorological processes associated with basin cold-air pools in which lower-atmospheric stability suppresses mixing and dilution processes (Doran et al. 2002). One of the instrument systems deployed to the center of the GSL basin during VTMX was a scanning Doppler lidar system, which mapped out the basin flow fields.

At the scale of the basin, the Doppler lidar found a recurrent, diurnally varying along-basin flow under periods of light synoptic forcing. This within-basin flow was from the north during the day, reversing to a southerly down-basin direction at night. The southerly flow

Corresponding author address: Robert M. Banta, NOAA (ET2), 325 Broadway, Boulder, CO 80305.
E-mail: robert.banta@noaa.gov

generally featured a low-level jet (LLJ) structure. The lidar showed this jet to be the dominant flow feature in the basin, and its presence altered or modified other processes and flows that would be expected in the absence of the jet. In the present study we investigate the nighttime development of this down-basin jet, its night-to-night variation, its vertical structure, and its relation to the larger-scale surface pressure gradient. The development of smaller-scale local, thermally forced flows was among those processes affected by this basin-scale flow, and so we also address the relation between the basin-scale jet and the slope-flow and canyon-outflow development along the Wasatch Range, which forms the eastern boundary of the basin. The coexistence of the basin-scale jet with the slope and canyon flows produced local regions of convergence, which led to localized upward motions. These effects were studied numerically, and the model results are also described. Last, the GSL basin is connected to the Utah Lake basin to the south by a gap at Jordan Narrows. Characteristics of the flow entering the GSL basin through this gap are described and compared with measurements in the center of the GSL basin.

In Part II of this study, the effects of the evolution of this nocturnal down-basin jet on the dispersion and distribution of tracer material released in the vicinity of the Salt Lake City, Utah, urban center (Allwine et al. 2002) will be further investigated.

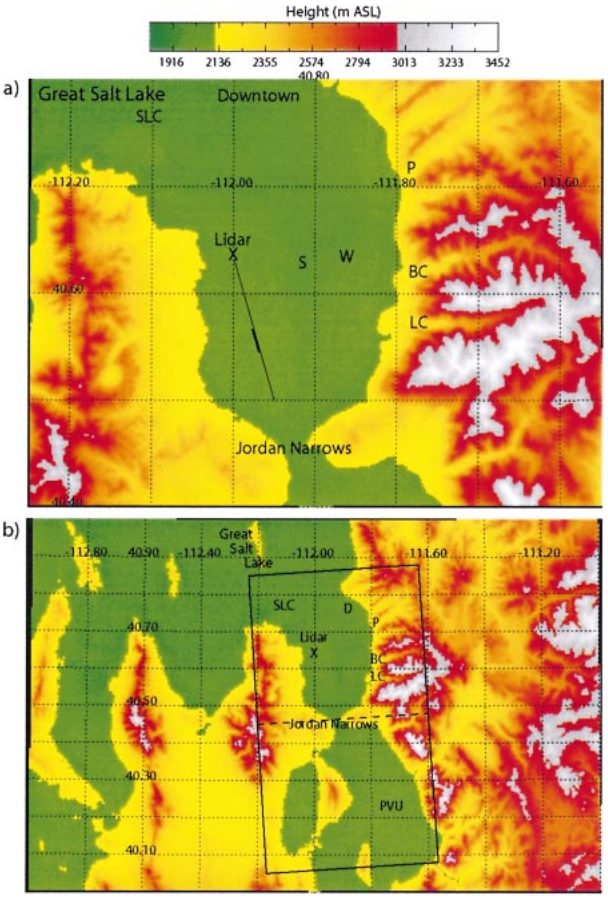

FIG. 1. (a) Map of the Salt Lake basin, showing the location of Salt Lake City (''Downtown'') and the Doppler lidar in the middle of the basin. Other features, including the GSL, canyon openings (P = Parley's Canyon; BC = Big Cottonwood Canyon; LC = Little Cottonwood Canyon), the midbasin PNNL profiler sodar site (S), the Wheeler Historic Farm rawinsonde site (W), the Salt Lake City International Airport (SLC), and Jordan Narrows, are indicated. The line extending from the lidar toward Jordan Narrows is the baseline of the vertical slice scans used in this study. The thick portion of this line extends from 7 to 9 km from the lidar and indicates the extent of the horizontal averaging used to determine profiles. Topography below 2100 m MSL is indicated in green. (b) Expanded map of region, showing the Salt Lake basin and its relation to the Utah Lake basin to the south and to other basins to the west. PVU is the site of the Provo Airport.

2. Background

The VTMX October 2000 campaign was organized to study meteorological processes responsible for vertical transport and mixing of mass, momentum, heat, contaminants, and other quantities under stable conditions (Doran et al. 2002). The study took place in the Great Salt Lake basin (Fig. 1) and thus addressed the formation, maintenance, and destruction of the nocturnal cold-air pool that formed in that basin, as well as the transport processes within the cold pool. Three important considerations for this study were 1) that it took place in an intermountain basin, 2) that the static stability of the inversion layer produced by surface cooling had a significant impact on the processes encountered, and 3) that the study basin is connected with other basins to the south via the Jordan Narrows gap.

First, the wide GSL basin has dimensions of ~30 km west–east and 45 km from the Jordan Narrows to the south shore of the GSL, where it is open to the north. The opening at Jordan Narrows seems small when compared with these dimensions. It was, therefore, assumed prior to the VTMX field campaign that the flows through this opening were small and localized, equivalent to assuming that the GSL basin would behave as a simple basin. Here, a simple basin is one in which processes occurring on length scales much larger than the basin (e.g., the LLJ) are unimportant. A basin with flows from tributary valleys and canyons is here regarded as a simple basin, provided the length scales of the valleys or canyons are not *much larger* than basin scale. Geometric aspects of cold pools in simple basins are discussed by Petkovšek (1978, 1980).

The essential nocturnal processes in a simple basin include the filling of the basin with a layer of cold air, or a cold pool, and the events that happen in the cold pool once it has been formed. Once the cold layer has formed in the basin, it is important to be able to characterize the vertical redistribution and dilution of atmospheric quantities, the stability of the cold-air layer (which is a product of the vertical redistribution of heat),

and the effectiveness of the horizontal transport and dilution within the cold pool.

Various aspects of this problem have been described in other studies. The contribution of drainage flows to filling the basin cold pool are described by Geiger (1965), Neff and King (1989), and Allwine et al. (1992), and the role of drainage flows in the transport of atmospheric tracer material within the cold pool was investigated by Allwine et al. (1992). Other studies of processes in mountain basins include Kao et al. (1975) in the Great Salt Lake basin; cold-pool development studies in smaller basins, including Colorado's Sinbad basin (Whiteman et al. 1996; Fast et al. 1996) and in Utah's Peter Sinks basin (Clements et al. 2003); and morning cold-pool breakup studies of Banta and Cotton (1981), Banta (1984, 1985, 1986), and Kelly (1988).

The second consideration is the static stability of the cold pool. The major effect of stability within this low-level inversion layer is to suppress mixing and, in particular, suppress the mixing out of small-scale phenomena within the basin. Examples of such small-scale features can include basin-scale features themselves, which are already at scales considered small for most purposes; subbasin scale features, such as layers and localized jets in addition to those portrayed in Fig. 2; and even smaller turbulence-scale features, which would include turbulence bursts, shear instabilities, waves and wave packets, finescale density currents, turbulent wakes of flow obstacles, etc. In the absence of significant overall mixing, these small-scale features persist, and they become the agents that perform most of the redistribution of airborne quantities (heat, momentum, trace species, etc.) under stable conditions. Because of the impact of such small-scale processes on transport and mixing, a study of stable boundary layer processes is, thus, necessarily a study of details.

Based on previous studies and the experience of the investigators, the basic processes were expected to include the following.

1) Basinwide layered processes would include inversion formation by surface-based radiative cooling, and shear-generated mixing by ambient winds at the top of the cold pool. The latter becomes less efficient as the ambient flow becomes weaker.
2) Downslope (drainage) flows off of the surrounding slopes and cold outflows from the canyons contribute to the formation of the cold pool.
3) Flows within the basin cold pool would be locally generated and, therefore, weak or shallow, except that tributary canyon outflows can be significant (Banta et al. 1995, 1997).
4) Horizontal transport would be limited because of the third process, except in canyon outflows, in thin slope-flow layers, or in local areas of upward motion, where cold-pool air could be lifted into the ambient flow.
5) Flows down major slopes would produce subsidence above the ridges; midbasin convergence of the slope flows or tributary outflows would produce a rising motion above the basin.
6) Vertical mixing within the cold pool mostly results from small-scale local processes such as those illustrated in Fig. 2. A key research need is to assess which of these processes have significant contributions to transport and mixing, and which have relatively minor roles.

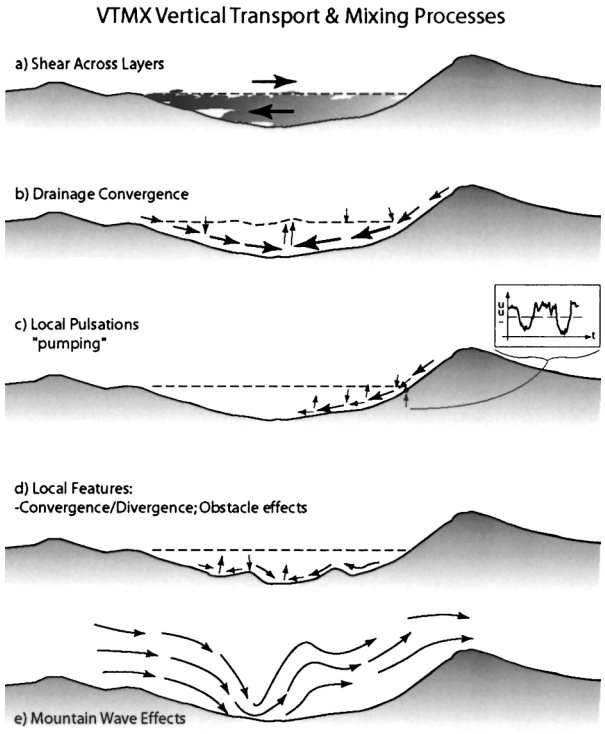

FIG. 2. Processes that can produce vertical transport or vertical mixing in a mountain valley or basin under stable cold-pool conditions. (a) Shear between the (often light) flow in the cold pool and the ambient winds aloft, or between flow layers within the cold pool, can produce waves and mixing. (b) Acceleration of drainage flows down slopes can produce divergence and draw air downward toward the surface. At locations midbasin, drainage flows converge, producing upward motion. (c) Nonstationarity of drainage flows along slopes are observed to produce pulsations, which in turn produce localized up and down motions. (d) Topographic features within the basin, such as hills, ridges, cliffs, barriers, ravines, etc., can produce *w* by acting as obstacles to the stable flow that forms in the basin, or by otherwise disturbing uniform flows, e.g., by convergent channeling effects, or by diverting or focusing drainage flows. (e) Wave effects downwind of the basin sidewalls or downwind of within-basin obstacles can produce significant *w* and vertical mixing. Also included in this effect would be upstream blocking of the stable flow by obstacles or barriers within the basin, which also produce *w* and mixing.

These processes were regarded as important in a basin where an along-basin jet was not a factor, because its existence as a recurring diurnal entity in the SLC (or any) basin was unknown prior to VTMX. Thus, for this study, it is important not only to characterize the jet,

but to consider how such a jet might change the picture in the basin.

In this study we also investigate effects of external processes, namely, the larger-scale pressure gradient forcing, on flows within the basin. Banta (1986) studied the influence of external ridge-top wind speed on the morning cold-pool breakup process, but otherwise little work has appeared on larger-scale influences on flows within basins. However, the third consideration, the joining of the GSL basin with basins to the south via the gap at Jordan Narrows, means that the connected basins acted in some respects as a channel or long valley. An indication of this was that data at the Jordan Narrows gap show that the flow passing through the gap exhibited a fully developed jet structure with speeds comparable to those in the midbasin (section 3f). Thus, studies of the relationship between flow in long, narrow valleys and external forcing may be of interest.

External forcing can consist of large-scale wind effects and pressure gradient effects. External wind effects include the influence of ridge-top winds on drainage flows within a valley (Davidson and Rao 1963; Gudiksen et al. 1992; Barr and Orgill 1989; Clements et al. 1989; Doran 1991), the effects of external ridge-top winds on the development of flows within the valley being studied (Hawkes 1947; Tyson and Preston-Whyte 1972; Whiteman and Doran 1993; King 1997), and the effects of channeling of the large-scale flow into a valley (see Whiteman 1990). Studies of pressure and pressure gradient effects include studies of the relationship between diurnal flow reversals and the pressure difference between a valley and the adjacent plain (Hawkes 1947; Nickus and Vergeiner 1984; Vergeiner and Dreiseitl 1987), a study of mountain flows and sea breezes across the Norwegian mountains (Sterten and Knudsen 1961; see Barry 1992, p. 170), and the relationship between the large-scale pressure gradient and the magnitude of along-valley flows (Whiteman et al. 1999).

Jetlike structures have been observed in long valleys using tethered balloons (Whiteman 1982) and remote sensing (Post and Neff 1986; Banta et al. 1996, 1997, 1999; Weissmann et al. 2004). Examples observed during VTMX included a Doppler lidar scan that exhibits strong southerly flow at low levels in the GSL basin (Doran et al. 2002), and time–height cross sections of profiler winds that showed nocturnal southerly flow in the midbasin on two nights (Zhong and Fast 2003).

Last, one of the original goals of the Doppler lidar deployment was to study basinwide budgets. The cold-pool mass budget would be evaluated by measuring the strength and depth of inflows into the basin from the slope flows, canyon outflows, and flow through the Jordan Narrows and out toward the Great Salt Lake. Because the movement of mass is an important aspect of other budgets, including heat and momentum, these mass budget studies were seen as key to understanding the other budgets. A facet of this goal was to assess the importance of small-scale vertical transport mechanisms, such as those shown in Fig. 2, in these budgets. A further goal in postanalysis, now that the basin jet has been identified as a major factor in the nighttime dynamics of the GSL basin, is to assess how the jet affects the ability to evaluate those budgets.

TABLE 1. Lidar specifications and parameters for VTMX.

Lidar specifications	
Wavelength (μm)	10.59
Max range (km)	Up to 30.0
Min range (km)	1.2
Range resolution (m)	300.0
Beamwidth (μrad) (°)	90.0 (0.005)
Rms velocity accuracy (cm s^{-1})	60
Nyquist frequency (MHz)	5.0
Pulse repetition frequency (Hz)	10
Pulses averaged	3.0
Effective pulse rate (Hz)	3.33
Standard scan rate (° s^{-1})	3.33
Angular resolution (°)	1.0

a. Doppler lidar

The present study makes extensive use of data obtained from the scanning CO_2 Doppler lidar developed and deployed by the Environmental Technology Laboratory (ETL) of the National Oceanic and Atmospheric Administration (NOAA). This lidar was deployed to the middle of the basin (Fig. 1) at an elevation of 1420 m. This instrument, because of its laser configuration [transverse-excited, atmospheric pressure, carbon dioxide (CO_2) laser] is referred to as TEACO2. It is described in detail by Post and Cupp (1990), and its use in complex terrain has been described in many other studies (Post and Neff 1986; Banta et al. 1995, 1996, 1997, 1999; Neff 1990; Levinson and Banta 1995; Darby et al. 1999).

Relevant characteristics of this lidar system during VTMX 2000 are listed in Table 1, including its range resolution (300 m) and velocity precision (60 cm s^{-1}). Scattering targets for the lidar are atmospheric aerosol particles, and so the strength of the signal is determined in part by aerosol properties, including concentration. One aspect of VTMX 2000 was that this particular October had anomalously clean air. An aerosol backscatter lidar had been operating for many years at the University of Utah (Sassen 1994), and 2000 was the cleanest October in 16 yr of data (K. Sassen 2001, personal communication). Particulate (PM-10) monitors also documented these unusually low aerosol concentrations, as reported by Doran et al. (2002). The effect of these low concentrations was that the range of the lidar was generally less than the 20+ km expected, based on the previous experiment at Colorado Springs, Colorado (Olivier and Poulos 1998).

ETL's TEACO2 Doppler lidar is a scanning system, capable of full azimuth and elevation scans. Although data from some nearly horizontal azimuth scans will be

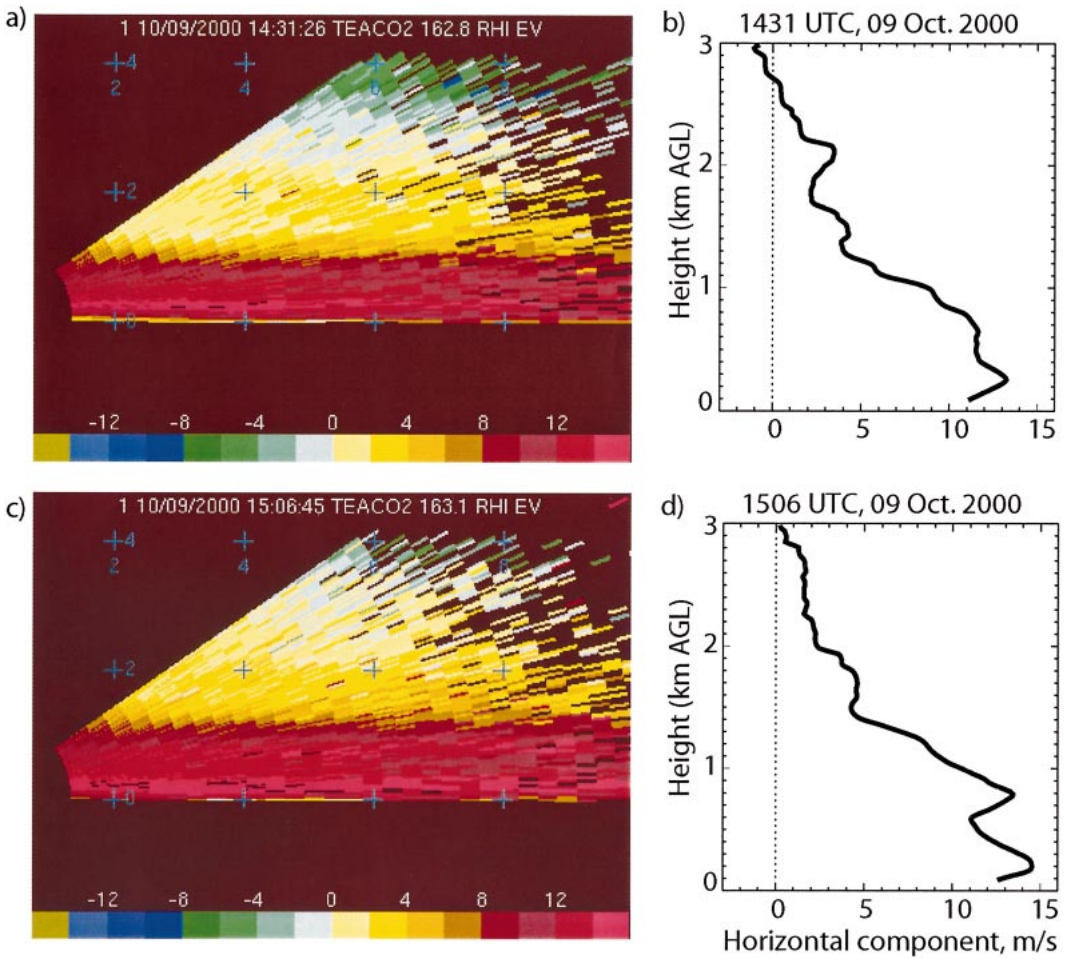

FIG. 3. (a) Range–height cross section of horizontal wind component in the plane of a Doppler lidar vertical slice scan taken toward Jordan Narrows at an azimuth of 162° at 1431 UTC 9 Oct 2000. Tick-mark crosses are 2 km apart. Color bar scale is from −16 to +16 m s^{-1}; positive values (yellow, red) indicate flow toward the lidar, and negative values (green, blue) indicate flow away from the lidar. The region between the 7- and 9-km range is the region where data were horizontally averaged to form profiles, as indicated by the thick portion of the line on Fig. 1. (b) Vertical profile of the horizontal wind component averaged between 7 and 9 km from the scan in (a). (c) Same as (a) except at 1506 UTC. (d) Same as (b) except taken from the cross section in (c) at 1506 UTC.

presented, most of the analysis will be from elevation scans pointed toward Jordan Narrows, the gap in the Traverse Range at the southern end of the basin. The baseline of these scans is indicated by a line in Fig. 1. Elevation scans, sometimes referred to as range–height indicator (RHI) scans, provide a vertical slice or cross section of the Doppler velocity field. Examples of such scans are shown in Figs. 3a and 3c. These scans were further analyzed by calculating the horizontal component from the radial velocity and interpolating to a Cartesian grid ($\Delta x = 150$ m, $\Delta z = 15$ m). We then averaged horizontally over the 14 interpolated data points at each vertical level from $x = 7$ to 9 km, to form vertical profiles of the mean lidar-determined horizontal wind component (as shown in Figs. 3b and 3d). These vertical profiles were further processed in two ways: 1) they were used to make time–height cross sections, and 2) the gridded velocity value at 90 m above lidar level (ALL) was plotted as a time series to track the behavior of the along-basin wind component.

b. Instrumentation at other sites

The instrumentation deployed during VTMX provided a significant enhancement to existing instrumentation in the GSL valley, which included a network of surface measurement sites—part of the MesoWest network as described by Horel et al. (2002)—and the twice-daily National Weather Service (NWS) rawinsonde ascents at the Salt Lake City International Airport (SLC). VTMX-deployed instrumentation and locations are described by Doran et al. (2002). They included UHF radar wind profilers, sodars, lidars, tethered balloons, additional rawinsonde ascents by the NWS and by project scientists

at two other locations in the basin, and several tracer studies using both SF_6 and perfluorocarbons (Allwine et al. 2002 and Fast et al. 2002, respectively). We note that during October significant migrations of birds occurred at night over the basin, occasionally degrading the performance of the radar wind profilers.

A 915-MHz wind profiling radar, with a radio acoustic sounding system (RASS) for virtual temperature measurements, was operated by the Pacific Northwest National Laboratory (PNNL) in the central Salt Lake valley at the site marked ''S'' in Fig. 1a. The measurement site was 7.25 km east of the lidar on a bearing of 96.6°. This phased array system sampled at two range-gate resolutions (60 and 200 m), using five beams in each mode. The RASS was operated for 5 min at the end of each half hour and sampled virtual temperature using 60-m resolution. Vector wind profiles were provided from the radar data for each half-hour interval in postprocessing using the National Center for Atmospheric Research (NCAR) Improved Moment Algorithm (NIMA; Cornman et al. 1998; Morse et al. 2002). NIMA was also used to provide 7-min samples of the wind field from individual sequences through the five radar beams.

In addition to the wind profiler, PNNL also operated a single-axis minisodar and a sonic anemometer at the site. The minisodar measured profiles of vertical velocity with 5-m spatial resolution and approximately 0.5-s temporal resolution to a height of approximately 100 m. The sonic anemometer measured the wind vector and virtual temperature at a height of 8.5 m with a sampling rate of 10 s^{-1}.

To monitor characteristics of the flow entering the basin from the south through the gap, a significant complement of in situ and remote sensing instrumentation was deployed to the vicinity of Jordan Narrows by researchers from the Atmospheric Technology Division (ATD) of NCAR. The site was located approximately 19.7 km from TEACO2 at an azimuth of 160°. The NCAR site, which was situated in a gully at an elevation of 1372 m, was, thus, somewhat lower than TEACO2. The NCAR Integrated Sounding System (ISS), which includes a surface station and rawinsonde sounding system, was enhanced with several remote and other sensing systems to meet the scientific objectives of the VTMX field campaign. These additions included a second surface station located on a nearby hill (30 m above the main site), a backscatter lidar [the scanning aerosol backscatter lidar (SABL), which was deployed in a nonscanning ground-based mode], a Meteorologische Messtechnik (METEK) minisodar, and the balloonborne tethered atmospheric observing system (TAOS). Radiosondes were launched every 2 h during intensive observing periods (IOPs). This enhanced complement of instrumentation enabled near-continuous sampling of the nocturnal boundary layer. Located on the periphery of the effective range of the ETL Doppler lidar, this site provided important information on the vertical structure of flow entering the GSL basin from the south.

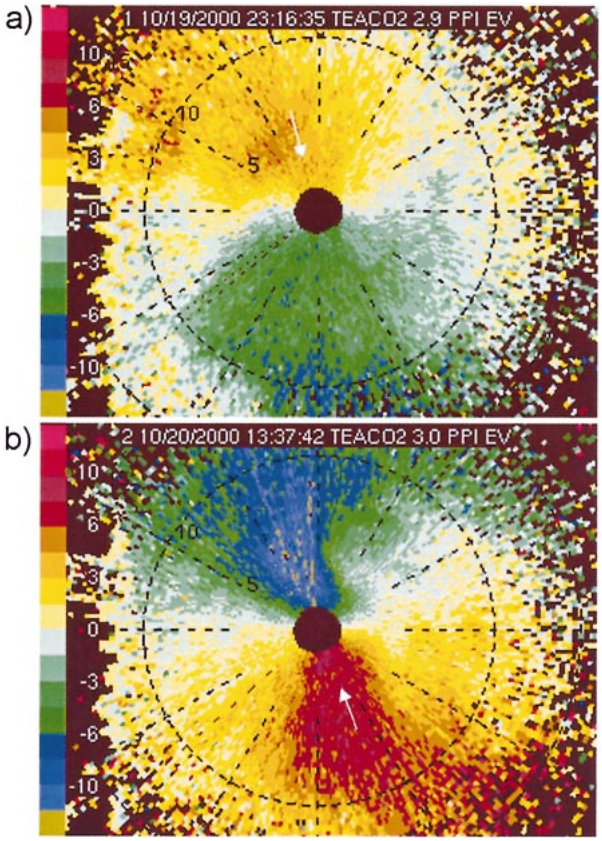

FIG. 4. Conical Doppler lidar azimuth scans at 3° elevation showing radial wind velocity as a function of azimuth (north is up, east is to the right). (a) Afternoon scan at 2316 UTC at the start of IOP 8, showing daytime up-basin flow. (b) Early-morning scan at 1337 UTC on 20 Oct (IOP 8), showing a down-basin jet resulting from an entire night of surface cooling. White arrows indicate direction of flow, sign of velocities and color bar are as in Fig. 3, and dashed ring indicates a range of 10 km.

The official time for the project was the coordinated universal time (UTC), which is 7 h ahead of local mountain standard time (MST). The times of sunrise and sunset during the project ranged from 1333 and 0101 UTC, respectively (0633 and 1801 MST), on 6 October to 1354 and 0030 UTC (0654 and 1730 MST) on 26 October, the last day of the project, using calculations based on the Whiteman and Allwine (1986) solar algorithm.

3. Results

An example of the along-basin flows revealed by low-angle azimuth scans from the Doppler lidar is shown in Fig. 4. Figure 4a shows the northerly up-basin daytime regime, which reversed to southerly down-basin flow at night (Fig. 4b). The daily recurrence of this reversal indicates that these flow systems were driven by the heating and cooling cycle at the earth's surface. The nocturnal basin-scale jet occurred most strongly aloft at a height of 30–200 m above ground level (AGL), and it sometimes exhibited a dual maximum in the vertical

direction (Figs. 3c,d). Often the true nature and strength of this flow were not evident from the surface data, because under stable conditions the flow aloft is frequently decoupled from the flow at the surface (see, e.g., Fig. 6b of Doran et al. 2002 or Fig. 8 of Zhong and Fast 2003). In this section we investigate the temporal behavior of the along-basin flow component and its relationship to pressure gradients outside and within the basin. We also address the effect of the jet on the Wasatch Mountains slope and canyon flows, its role in producing localized regions of divergence and vertical motion, and its behavior passing over the gap at Jordan Narrows.

The diurnal behavior of the low-level winds is also consistent with lake-breeze forcing, and, in fact, a flow reversal similar to a lake-breeze front was detected moving southward through the basin on some light-wind days. At night, however, land breezes are typically shallow, weak, and difficult to detect and are strongest near the surface (Atkinson 1981). Thus, the strong down-basin jet observed was not caused by the land–lake temperature contrast to any significant degree, and it is attributed here to forcing by pressure gradients induced by cooling of the terrain surface.

a. Evolution of down-basin jet

Figure 5 shows the along-basin component of the flow as a function of the time of day for the seven most completely studied IOP nights of VTMX. This figure displays in color the data interpolated to the 90-m height ALL and horizontally averaged as described in section 2a. Also plotted is the large-scale north–south pressure difference across the basins, determined from the hourly reported sea level pressure (SLP) between Price, Utah, to the south and Pocatello, Idaho, to the north. In this figure a negative difference indicates high pressure to the south, thus, favoring down-basin (southerly) flow. Although other ways of expressing surface pressure would be preferable to SLP in complex terrain (Steinacker 1988), we regarded SLP as an adequate indicator of the large-scale pressure difference for present purposes.

According to Fig. 5, daytime up-basin (positive) flow reversed to nighttime down-basin flow typically 2–3 h before midnight at local standard time (0700 UTC) on nights when the magnitude of the large-scale pressure difference was not too strong (less than ~3 hPa, as during IOPs 4–6,8). Also shown is a night when the pressure difference was large and positive for the entire period (7 October, IOP 2), and another night when the difference was large and negative (26 October, IOP 10). The strong larger-scale pressure gradient in both cases produced flows that were driven synoptically and, thus, did not respond to the day–night reversal of the thermal forcing. On these nights the low-level flow, confined within the basin complex, blew from higher to lower surface pressure through the multibasin channel. During IOPs 2 and 3 the pressure-driven flows appeared as windstorms from the canyons in the northeast sector of the basin (Holland 2002).

On nights when the larger-scale pressure gradient was weaker and a transition from up- to down-basin flow was observed, the timing of the reversal was related to the pressure difference, and night-to-night variations can be noted. On 15 and 17 October (IOPs 5–6) the larger-scale pressure gradient was weak but favored down-basin flow (indicated as negative), and the reversal occurred 2–2.5 h before midnight on both nights. On 18 October (IOP 7) the pressure difference was in the same sense but stronger, and the reversal occurred 4 h before midnight—earlier than on the previous two IOP nights, which had the weaker gradients. 9 October (IOP 4) was a synoptically transient night, on which the larger-scale pressure difference was weakly positive and reversed at midnight. The flow itself, however, reversed well before midnight. The overall relation between the timing of the flow reversal and the large-scale pressure difference is summarized in Fig. 6. The behavior is reasonably linear, if we disregard the anomalous behavior from transient synoptic conditions during IOP 4.

A curious feature of IOPs 5 and 6 was a decrease in the magnitude of the down-basin flow and pressure differential after 0900 UTC, followed by a recovery of the down-basin flow after ~1200 UTC. The reduction of the down-basin flow speed was related to the decrease in the pressure gradient, but the reason for the pressure gradient decrease is a subject requiring further study. Data near the Jordan Narrows gap for these nights (section 3f) suggest that larger-scale influences may have a role.

The weakest pressure differential occurred on 20 October (IOP 8), which began with a slightly positive difference. Of all the cases during the VTMX 2000 campaign, the low-level flow within the basin on this night was thus probably the most representative of pure thermal forcing of the nocturnal flows. Indeed, the slope flows and canyon outflows from the Wasatch Range to the east were especially strong on this night (e.g., Fig. 7). However, a down-basin jet did form at about midnight (0700 UTC), and, although the reversal was significantly later than on IOPs 4–7, its strength became comparable after it formed. Figure 7 shows the coexistence of both of these types of flow systems in the early morning hours, after the basin jet had formed.

b. Within-basin pressure evolution

The Price–Pocatello SLP difference represents a synoptic-scale pressure gradient imposed on the overall basin complex, but within the basin the day–night flow reversals are driven by a more local-scale pressure differential, which varies diurnally. To investigate the behavior of this local within-basin pressure gradient, we plotted hourly altimeter-setting differences for two stations within the basin complex, the Salt Lake City International and Provo

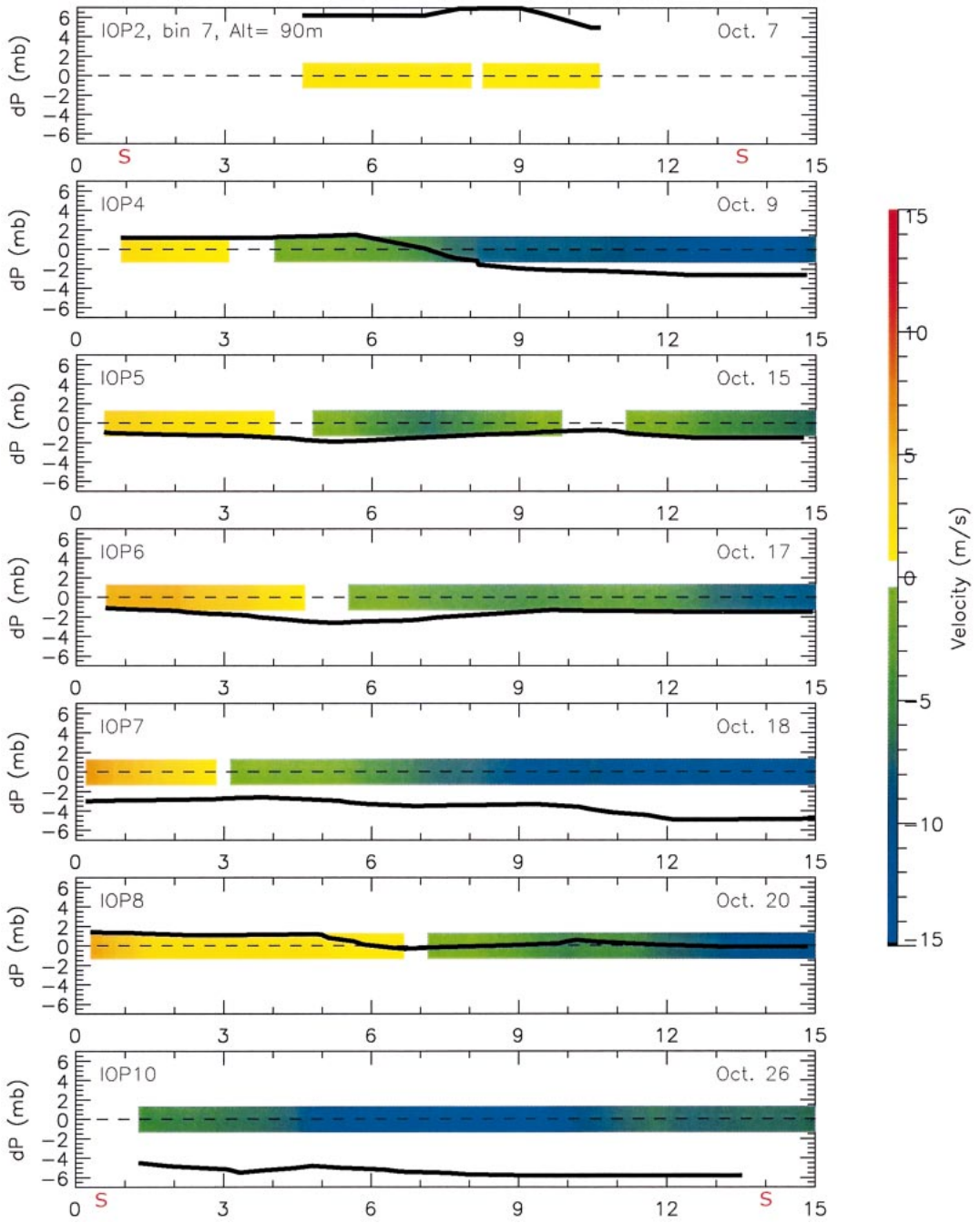

FIG. 5. Time series plot of along-basin wind component [color bar on right (m s^{-1}); positive values indicate up-basin (northerly) flow] at 90-m height averaged along the thick, solid bar in Fig. 1 for seven IOPs during Oct 2000. Solid black lines indicate sea level pressure difference between Price, UT, and Pocatello, ID. Scale at left is in hectopascals, and negative values indicate higher pressure to south. Abscissa is hour UTC. Red Ss under the axes to the left side of top and bottom panel indicates times of sunset; those to the right side indicate times of sunrise.

(SLC and PVU, respectively) Airports. Because the altimeter setting is calculated by a constant, standard atmosphere reduction to sea level, it is a truer indicator of hour-to-hour variations in pressure than is SLP. The SLC–PVU pressure (altimeter) differences are plotted in Fig. 8 for the seven nights shown in Fig. 5. Also shown is a trace of the lidar midbasin winds as given in color in Fig. 5. The pressure difference started out near zero on nights that had a flow reversal, and then decreased through the night by 1–2 hPa (0.03–0.06 in. Hg). The timing of the reversal of the flow, indicated by arrows on Fig. 8, occurred about when the SLC–PVU difference

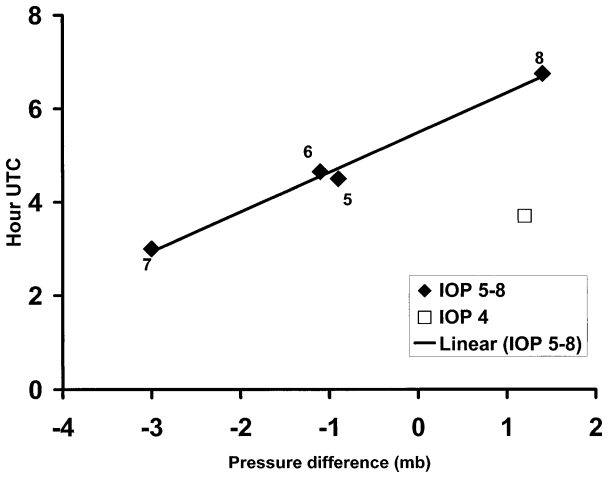

FIG. 6. Time of evening flow reversal (UTC) plotted as a function of the large-scale Price–Pocatello pressure difference (hPa) at 0000 UTC. Numbers next to diamond data symbols indicate IOP numbers for IOPs 5–8. Open square shows data for IOP 4, when synoptic conditions were in transition from windstorm conditions of IOPs 2 and 3 on the previous 2 days to more settled conditions.

crossed over −0.7 hPa (−0.02 in. Hg). The data presented in Figs. 5 and 8, thus, represent two different scales of pressure gradient that affect the behavior of the low-level wind in the GSL basin. Figure 5 represents the background larger-scale pressure gradient, superimposed over the diurnally varying pressure differential within the basin, which is illustrated in Fig. 8.

The pressure traces in Fig. 8 show significant changes over ~1 h, as a result of cooling of slope surfaces and the filling of the basins with cold air. The dominant dynamics here are, thus, the acceleration of the flow in response to this changing pressure gradient. The time scale is too fast for Coriolis effects to be a significant factor. The Coriolis time scale is the inertial period (half-pendulum day), which at this latitude is nearly 16 h. Thus, the geostrophic adjustment dynamics that produce the Great Plains LLJ are not a major influence here.

c. Vertical structure

In addition to the down-basin jet and its relationship to surface pressure gradients, it is of interest to investigate the depth of influence of this basin-scale thermal forcing and to determine to what extent the ridge-top-flow component aloft may have been changing. Time–height cross sections were produced from Doppler lidar vertical slice scans following the procedure described in section 2. Cross sections for the nights with a flow reversal (IOPs 4–8) are shown in Fig. 9.

Diurnal thermally forced flow influences within the basin showed up mostly below 1 km ALL, whereas changes in the large-scale ridge-top winds appeared above 1 km. For example, IOP 7 (Fig. 9d) had a relatively strong down-basin pressure difference throughout the observation period (Fig. 5), and as a result, the flow above 1 km showed a consistently southerly (negative) component. Below 1 km (i.e., within the basin), and especially below 600 m, daytime up-basin flow (positive) yielded to nighttime down-basin flow at 0300 UTC. IOPs 5 and 6 (Figs. 9b,c) also exhibited a distinct reversal of flow direction within the basin, especially below 500 m; above 1 km ALL the along-basin component was variable in direction, but the speeds were persistently light. During IOP 4 the change in the sign of the pressure difference (cf. Figs. 5, 8) and the transient synoptic conditions are reflected here as an early (before ~0100 UTC) shift in wind direction above 1 km ALL and a continued strengthening of this flow through the night. The flow aloft during IOP 8 showed a steady veering from northwesterly to southeasterly through the night as indicated by velocity azimuth display (VAD) analyses of the lidar data (not shown). The veering is reflected here as a shifting of the component in this layer from northerly to southerly between 1 and 1.5 km ALL. This ridge-top wind shift had a significant influence on the flows emerging from the canyons in the Wasatch Range, which is the subject of another study in progress.

Data from the profiler–sodar site in the Jordan River valley (site ''S'' in Fig. 1a) were mostly consistent with these results (Shaw et al. 2003). In particular, the flow regimes and timing were in good agreement for IOPs 6, 7, and 8, and the strong southerly flow after midnight local time during IOP 4 was well represented in both datasets. Some discrepancies were also noted, the most significant being strong northerly winds indicated by the profiler on IOP 5. We noted in section 2 that significant migration of birds can occur at night over the basin in October, and this effect on radar wind profiler performance may explain the discrepancies during IOP 5. The profiler data also showed that some of the light-wind periods indicated by the lidar cross sections were periods of easterly or westerly flow, that is, perpendicular to the plane of the lidar scan.

Serial radiosondes launched each night (except IOP 6) from the Wheeler Historic Farm site in Utah (site ''W'' on Fig. 1a) in the middle of the basin showed the expected cooling with time below ~300 m AGL. With the onset of the southerly flow above 300 m (but below 1 km AGL), the profiles indicated a warming on the order of 1°C. This warming was not evident during IOP 8, however.

Generalizing the results in Fig. 9 does not seem to be straightforward. On two nights (IOPs 6 and 8) the down-basin flow started near the surface and deepened, as might be expected from pure thermal forcing at the surface, whereas on three of the nights (IOPs 4, 5, and 7) the transition was nearly simultaneous through at least the depth of the basin. This indicates a likelihood that other effects, such as ridge-top winds or other larger-scale processes, have a role in modifying the response of the basin to the diurnal heating cycle.

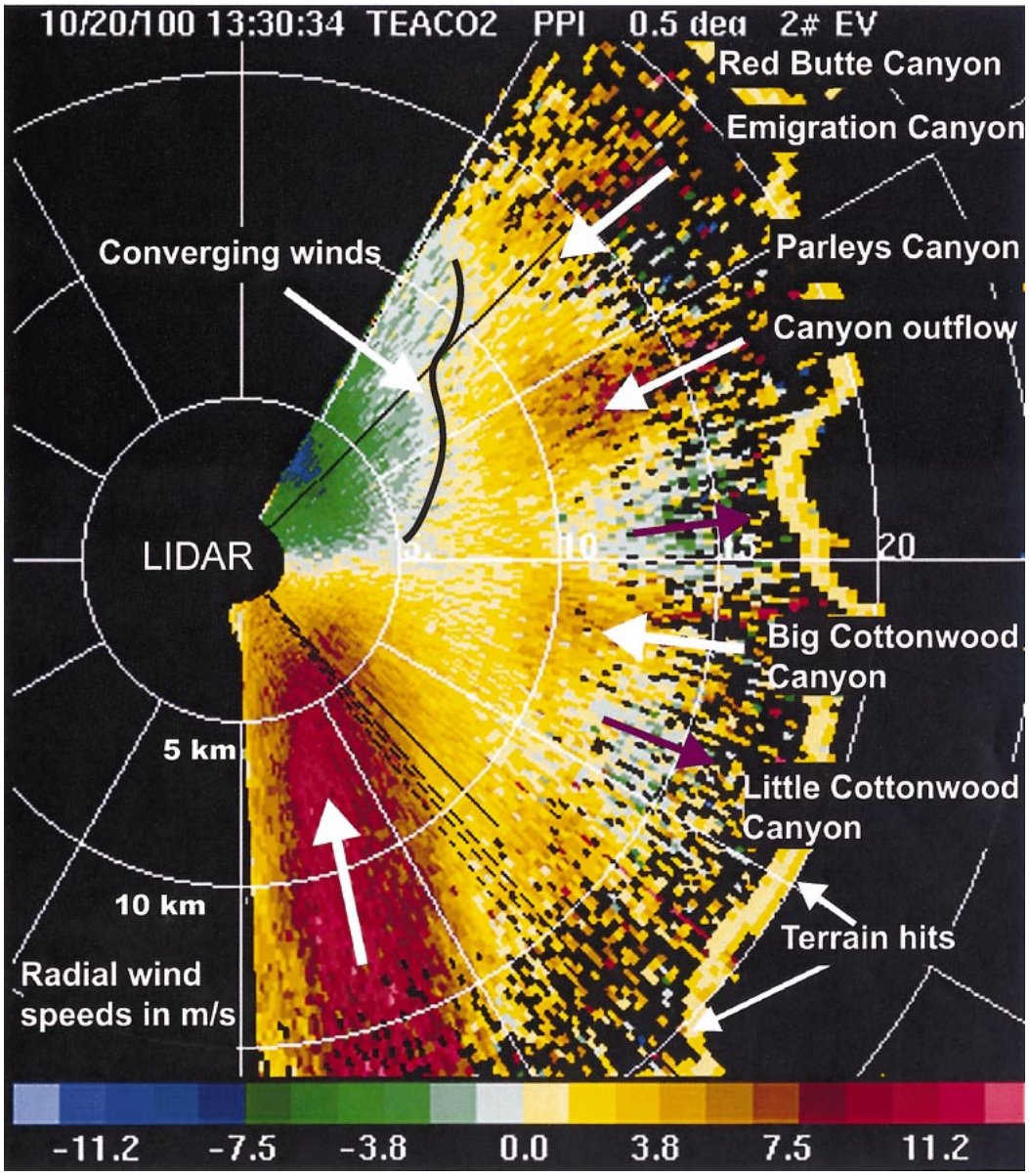

FIG. 7. Nearly horizontal azimuth scan (0.5° elevation) from Doppler lidar, taken at 1330 UTC (0630 MST) on 20 Oct (IOP 8). Range rings are at intervals of 5 km and velocities on the color bar are in meters per second (sign convention as in Fig. 3). Solid returns at 13–15-km range to the east indicate terrain hits, and the major canyons are annotated on the figure. North is up, and the Doppler lidar is located at (0,0). Figure shows down-basin jet coexisting with outflows from the major canyons (white arrows), forming a convergence line (wavy line to the northeast of the Doppler lidar).

d. Relationship to slope and canyon flows

Local thermally forced flows on a smaller-than-basin scale included katabatic flows down the slopes of the Wasatch and Oquirrh Mountains and canyon-outflow jets from the Wasatch canyons. These flows were easily recognizable in the Doppler lidar scan data (Figs. 7, 10). The outflow jets were similar to those studied in the Front Range of Colorado by Banta et al. (1995, 1996), Levinson and Banta (1995), Doran (1996), and Darby et al. (1999). Figure 7 shows that on the night with the weakest larger-scale pressure difference and the latest reversal, 20 October (IOP 8), these flows were strongly developed along the eastern portions of the basin, and they penetrated well into the center of the basin.

In contrast to this case were the conditions on 26 October (IOP 10), when a strong down-basin pressure difference was too strong for daytime up-basin flow to form, and the flow was down basin even during the prior daytime period. The effect of the nocturnal forcing was merely to increase the strength of this down-basin

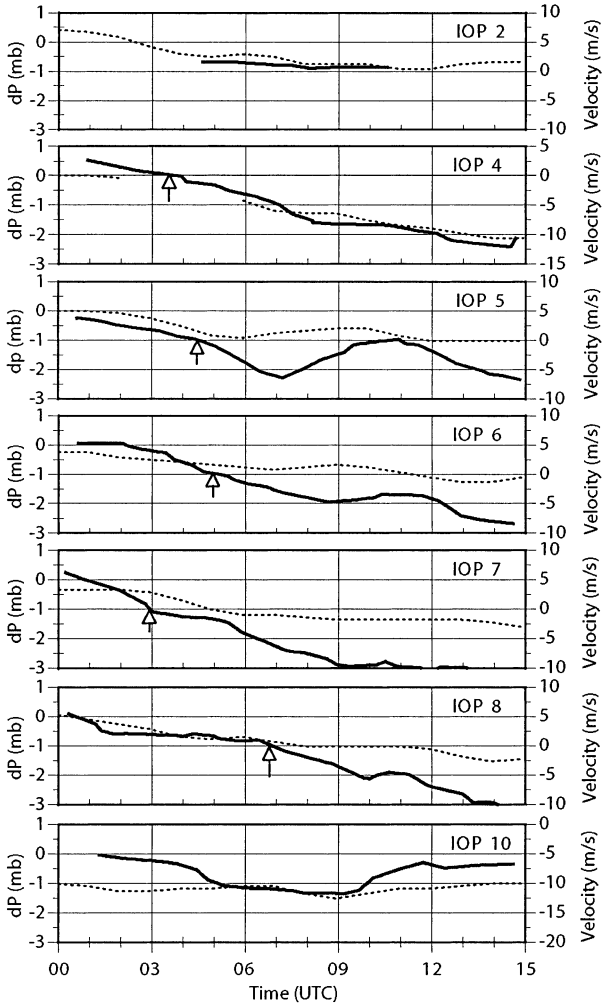

FIG. 8. Altimeter setting difference (dotted line) between Salt Lake City International and Provo Airports (hPa, scale to the left), plotted vs time (UTC) for seven IOPs during VTMX. Positive difference indicates higher pressure to the north. Also plotted are the same Doppler lidar–determined wind components (black line; m s^{-1}, scale right), as plotted in color on Fig. 5, vs time. Arrows indicate the times of zero crossings in the along-basin wind component curve.

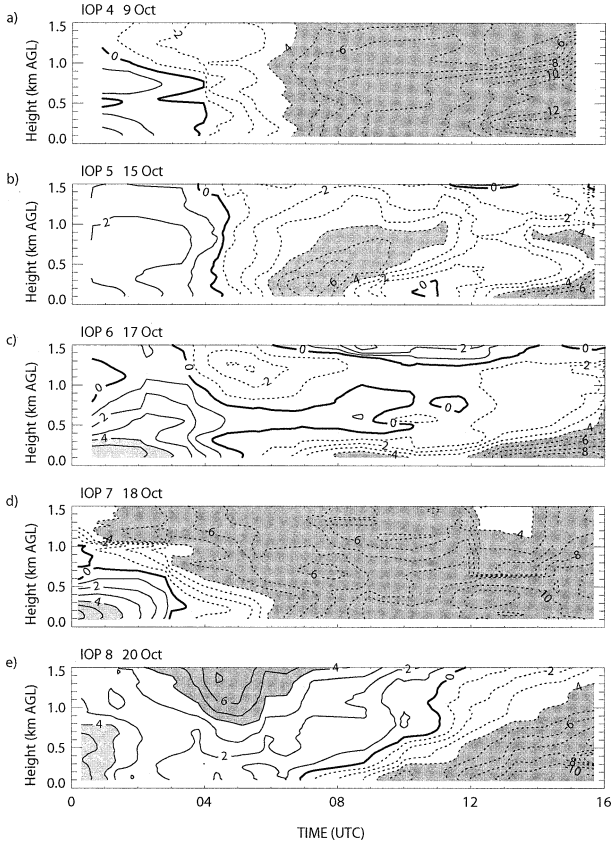

FIG. 9. Time–height cross sections of the along-basin wind component (positive = up basin) derived from Doppler lidar profiles as illustrated in Fig. 3. Data are shown for each of the five IOPs when a reversal from daytime up-basin to nighttime down-basin flow occurred after sunset. Abscissa is hour (UTC), ordinate is height above lidar (km), and contours are at 1 m s^{-1} intervals. Light shading indicates velocities greater than 4 m s^{-1}, and dark shading, less than -4 m s^{-1}.

flow (Figs. 5, 8). In particular, no reversal of flow occurred. This is significant, because on evenings when such a reversal did occur, it was associated with about a 2-h period of light and variable flow in the basin. Such a weak wind interval was favorable to the buildup of a cold-air inversion layer near slope surfaces and the consequent formation of thermally induced slope and canyon flows. An example of such local flows penetrating well into the basin during the light-wind period is shown in Fig. 10a.

During IOP 10 no such light wind period occurred, and the persistent, strong southerly basin-scale flow impeded the cold-air build-up processes responsible for the generation of the smaller-scale thermally forced flows. The stronger winds mix the cooling over a deeper layer and prevent strong cooling of the air next to the surface. Similar effects on drainage flows in valleys have been noted as a result of strong external ridge-top winds (Gudiksen et al. 1992; Coulter and Gudiksen 1995). Thus, those thermally forced slope and/or canyon flows that did form on this night were weak, disorganized, and exhibited minimal penetration into the basin. Figure 10b shows an example of these weak intermittent flows when they appeared during IOP 10, barely reaching the eastern edge of the lidar scan at a range of ~12 km.

During the IOPs that did have nocturnal flow reversals, Doppler lidar scan data showed that slope and canyon flows formed, but not as strongly as during IOP 8. Even during IOP 7, when the pressure difference was somewhat stronger than the other nights and the reversal occurred early, definite slope and canyon flows formed. The differences in the appearance of these small-scale flows between IOPs 7 and 10 are a critical factor in explaining the differences in the transport and dispersion behavior of atmospheric tracer (SF_6) released in the SLC

urban area, as will be demonstrated in Part II of this study.

Thus, under persistent, strong southerly flow with no light wind reversal period, the processes leading to small-scale thermally forced flows were suppressed. Any slope/canyon flows that formed were weak and disorganized, and were confined to locations close to the mountains. Conversely, when such a light wind transition period did exist and did lead to strongly established canyon outflows, these flows could penetrate into the middle of the basin and displace the southerly flow of the basin-scale jet well to the west, producing a convergence (and updraft) line as indicated on Fig. 7.

e. Convergence and upward motion effects

The reversal of the radial velocities northeast of the Doppler lidar in Fig. 7 indicates a line of convergence (wavy line) between the southerly jet and the easterly canyon outflows. Such low-level convergence is expected to produce significant vertical velocity *w*. This feature is similar to the local convergence processes illustrated in Figs. 2b and 2d, although this mechanism is probably stronger and more focused than those that would appear in a simple basin.

To quantify the *w* patterns throughout the basin, version 4.3 of the Regional Atmospheric Modeling System (RAMS) mesoscale model (Pielke et al. 1992; Fast et al. 2002) was run for IOP 8 (20 October). As described in Fast and Darby (2004), the turbulence parameterization employed consists of a simplified second-order closure method that employs a prognostic turbulence kinetic energy (TKE) equation (Mellor and Yamada 1982; Helfand and Labraga 1988). Condensation to cloud water vapor was included in the simulation, but the cumulus and cloud microphysics parameterizations were not activated because of the mostly clear conditions observed during IOP 8. The shortwave and longwave parameterizations (Chen and Cotton 1983) take account of cloud effects to determine the heating or cooling caused by radiative flux divergences. Turbulent sensible heat, latent heat, and momentum fluxes in the surface layer were calculated from similarity equations. Prognostic soil–vegetation relationships were used to calculate the diurnal variations of temperature and moisture at the ground–atmosphere interface. For the outer grids, vegetation type was based on a 1-km U.S. Geological Survey (USGS) dataset, while a more recent 100-m USGS dataset was used for the inner grid, which also had a more realistic distribution of urban land use.

Five nested grids were used with horizontal grid spacings of 45, 15, 5, 1.7, and 0.56 km. The outer grid covered the western United States, and the inner grid covered the Salt Lake valley and surrounding mountains. The model uses a terrain-following vertical coordinate, and in this study the vertical grid spacing gradually increased from 15 m adjacent to the surface to 500 m near the model top at 12 km MSL. Because of the staggered vertical coordinate, the first model grid point was 7.5 m AGL. The model was initialized at 1200 UTC 19 October for a simulation period of 36 h. Initial and boundary conditions were based on the National Centers for Environmental Prediction AVN model and on the operational, 12-hourly upper-air soundings. The GSL water temperature was set to 14°C, based on observations made during the period.

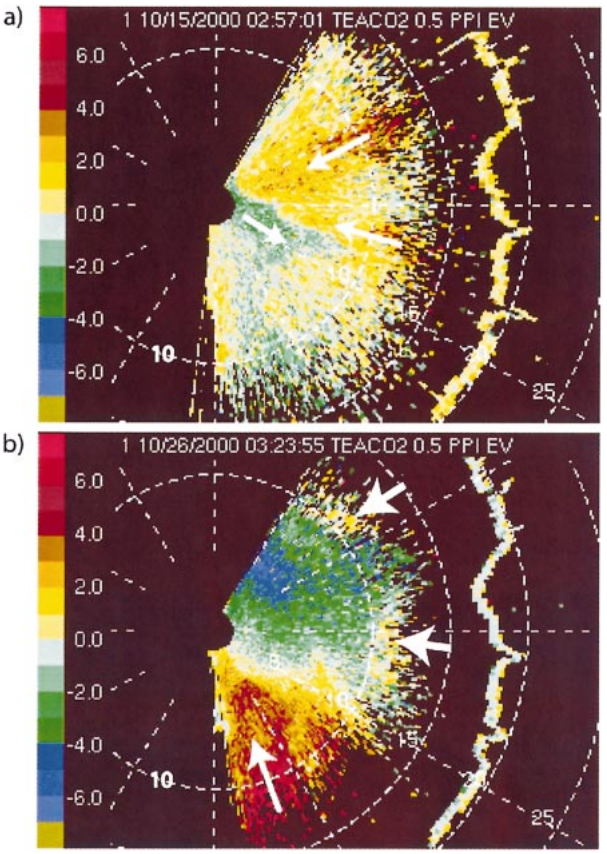

FIG. 10. Nearly horizontal (0.5° elevation angle) Doppler lidar azimuth scans as in Fig. 7. (a) Scan showing thermally forced canyon outflow surges penetrating far to the west toward the lidar from major canyons (long white arrows). Scan was taken during the light-wind transition period at 0257 UTC 15 Oct (IOP 5). Small white arrow indicates a component of the light wind flow near and to the south of the lidar. (b) Scan showing strong (7 m s^{-1}) southerly flow (long white arrow) at 0323 UTC 26 Oct (IOP 10), at a time of the evening when light and variable transitional flow was occurring during other IOPs (4–8). Short white arrows indicate weak canyon outflows barely reaching the edge of the lidar scan. Such outflows were shallow, and many similar scans on this night did not show evidence of canyon flows.

Similar simulations for eight of the IOPs were performed by Fast and Darby (2004) to show that the model errors were usually associated with the timing, structure, and strength of specific flows. The lidar measurements provided a means of systematically evaluating the predicted spatial structure of the circulations that could not be obtained from the point measurements alone. An example of the model results for IOP 8 is shown here to

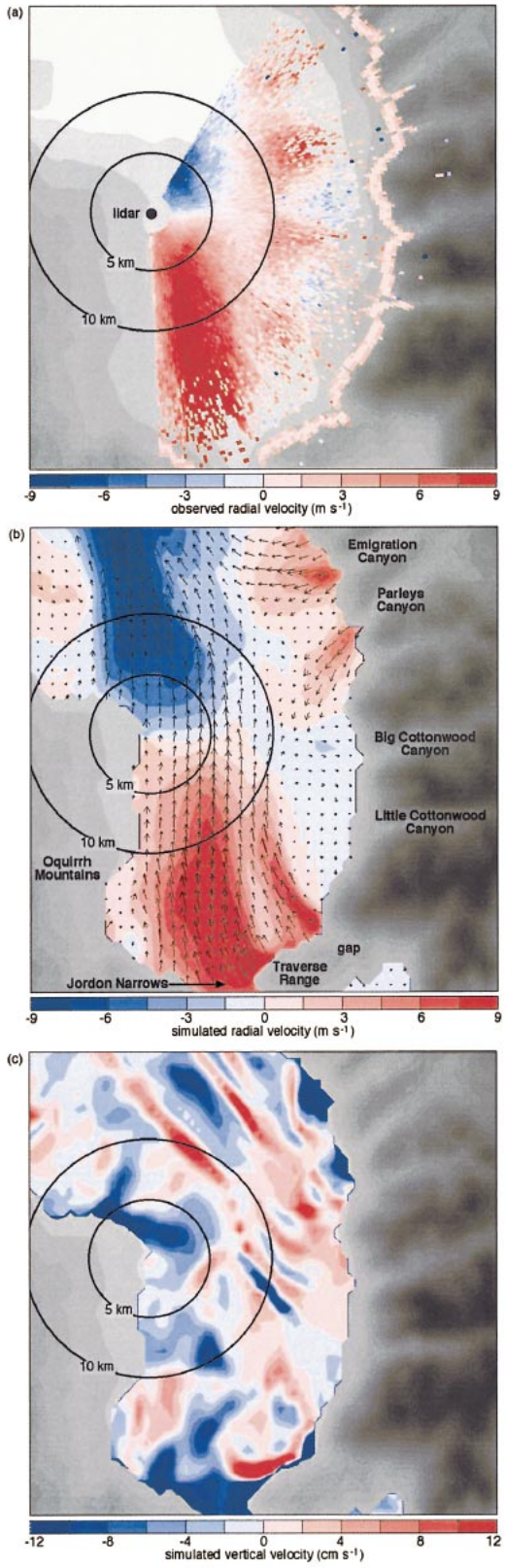

illustrate the magnitude and pattern of mean vertical motions associated with the southerly jet.

The simulated lidar-centered radial velocities at 1330 UTC are shown in Fig. 11b. They were obtained by first computing the radial velocities at each model grid point based on the lidar location, then interpolating the velocities vertically to correspond to the 0.5° elevation scan made by the lidar. They are to be compared with the lidar Doppler velocity scan data shown for the same time period in Figs. 7 and again in Fig. 11a. Also shown are horizontal wind vectors that depict the total simulated wind direction. The predicted radial velocity patterns are similar to the lidar measurements and to radiosonde and radar wind profiler measurements (not shown). The model indicates that the down-basin jet extended from the southern end of the valley to the Great Salt Lake and that the outflows from Parley's and Emigration Canyons were confined to the eastern side of the valley, in agreement with the Doppler lidar measurements (Figs. 7 and 11a). It is interesting to note that the wind speed maximum associated with the channeling of the flow through the small gap in the southeastern edge of the Traverse Range (to the east of Jordan Narrows, marked ''gap'' on Fig. 11b) was also observed by the lidar. The largest discrepancies between the model and the lidar occurred in the southeastern sector of the valley. An eddy was predicted in this region with light westerly winds just east of Big Cottonwood Canyon. The lidar, however, indicated a strong easterly outflow from Big Cottonwood Canyon that converged with the down-valley flow. The model did predict outflow from Big Cottonwood Canyon at higher-elevation scans (not shown), but the model wind speeds were still weaker than those observed. Fast and Darby (2004) show similar comparisons for other IOPs.

As shown in Fig. 11c, strong sinking motions (dark blue shading) were produced at many locations near and above the valley sidewalls, as the flow from the canyons descended into the valley. Over the northern end of the valley where the down-basin and Parley's Canyon flows converged, three narrow bands of rising motion exceeding 5 cm s^{-1} were simulated. Between these bands were regions of sinking motions with magnitudes also >5 cm s^{-1}. Other regions of large sinking motions were also produced along the down-valley flow over the center of the valley. A vertical wind speed of 5 cm s^{-1} seems small, but it is large enough to transport an air

←

FIG. 11. (a) Doppler lidar data from the same azimuth scan at 0.5° elevation as in Fig. 7, with color bar in meters per second. (b) Simulated Doppler lidar azimuth scan at 0.5° fixed elevation calculated from RAMS output as described in the text. Arrows indicate full horizontal wind vector on the simulated sloping scan surface. Color bar indicates the model-derived radial wind component that would be observed by a lidar at the location of TEACO2. This figure represents the same time and location as Fig. 11a. (c) Simulated vertical velocities (cm s^{-1}) for same time and location as Fig. 11b.

parcel 180 m vertically in 1 h, as pointed out by Doran et al. (2002). The converging flows persisted for several hours so that the contribution of the mean *w* to vertical pollutant transport is likely to be significant. Pollutants may be vented out of the nocturnal boundary layer by flows converging in the valley or may be trapped near the surface by divergent flows in other locations. The predicted mean *w* and turbulence in the valley suggest that regions of the stable boundary layer in the GSL basin may be periodically coupled with the air aloft during the evening. The model simulations showed converging flows in the basin for IOP 8 and five other IOPs (Fast and Darby 2004).

f. Gap flow behavior at Jordan Narrows

Measurements at the Jordan Narrows gap (surface stations, sodar, tethered balloon, and rawinsondes) show a jet entering the GSL basin from the south. Analysis products constructed from MesoWest surface observations suggest that the southerly nocturnal jet originated in the collection basins located to the south and southwest, including the Utah Lake basin just to the south, where the city of Provo is located (see Fig. 1b). It is of interest to compare the timing and strength of the southerly flow and the behavior of the temperature profile measured at the gap with those noted in the middle of the basin, to determine how the flow evolves as it emerges from the Jordan Narrows region. It is also of interest to study some details of the temporal behavior of the flow over the gap, as clues to which vertical mixing mechanisms may be acting.

The onset of the southerly jet at Jordan Narrows consistently occurred between 0400 and 0500 UTC (Fig. 12), whereas in the center of the basin, the onset time was more variable (Figs. 5, 8), probably because of a greater exposure to larger-scale forcing and ridge-top wind effects. A comparison of sounding, sodar, and TAOS (tethered balloon) data at the NCAR site in the gap with Doppler lidar data in the basin (as shown in Fig. 9) revealed subtle differences in the characteristics of the jet as it traversed the basin. On two occasions with a strong northerly pressure gradient (IOPs 2 and 3), jet structure was observed at the gap but not midbasin by the lidar. On nights when the jet was observed at both sites, peak wind speeds tended to be 0.5–2 m s^{-1} stronger at the NCAR site, probably as a result of the constriction of the flow as it passed through the gap. The shape of the speed profile was generally consistent between the sites, appearing either as a curve with a well-defined maximum or as a broad layer of relatively uniform high winds. Well-defined maxima were typically observed in the gap between 75 and 200 m AGL, somewhat lower than observed midbasin. The double maximum structure observed over the basin (Fig. 3d) was often seen in the gap as well.

Changes in the temperature profile during the shift to southerly flow at Jordan Narrows were less consistent

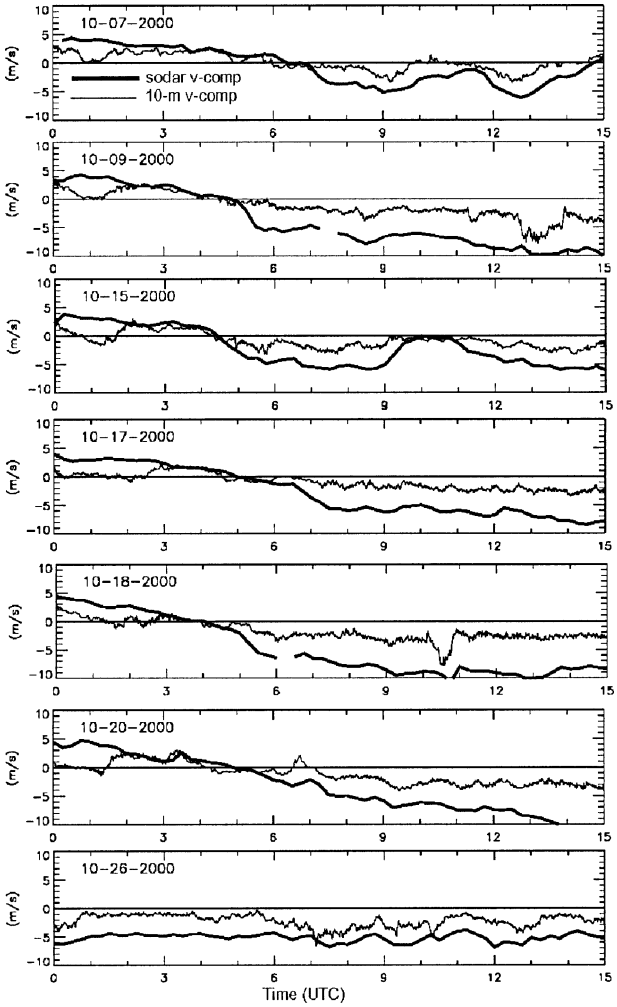

FIG. 12. Time series of northerly wind component (m s^{-1}) at the Jordan Narrows site as measured by the sodar (heavy black line) and by an anemometer on the 10-m tower (thin black line), plotted vs time (UTC) for the same IOPs and times as shown in Figs. 5 and 8. Sodar data are averaged over the lowest three range gates from 50 to 100 m AGL.

than observed midbasin. On some nights (IOPs 4, 5, 7) a thin (100–200 m) layer of transient warming of ~1°C was observed above the surface-based inversion layer after formation of the nocturnal jet (e.g., see 0300 and 0500 UTC profiles in Fig. 13). On other nights, however, the entire layer of air between the surface-based inversion and the free atmosphere showed consistent cooling through the night.

The temperature profile data did exhibit a consistent pattern at the lowest levels for the gap and midbasin as follows. When the winds below ~300 m AGL became light, as during the evening transition from northerly to southerly flow, the near-surface temperature cooled rapidly, as illustrated between the 0314 and 0458 UTC profiles in Fig. 13. Surface-based cooling increased the stability of the layer in the lowest 75–100 m, and, thus, a strong but shallow surface-based inversion layer was

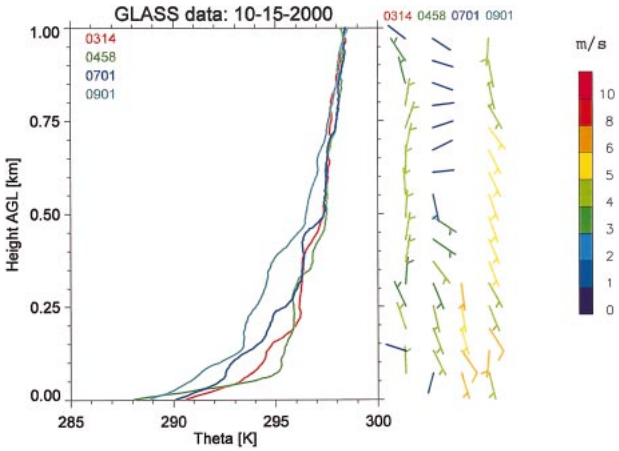

FIG. 13. Radiosonde soundings of potential temperature (K) vs height (km) at the Jordan Narrows site at 0314, 0458, 0701, and 0901 UTC on 15 Oct 2000 (IOP 5).

present prior to the emergence of the nocturnal jet. As wind speeds increased with the onset of the jet, the air temperatures below 75 m warmed and the strength of the inversion decreased, as shown between the 0458 and 0701 UTC soundings in Fig. 13. This warming was a result of enhanced vertical mixing caused by the shear below the nocturnal jet.

Low-frequency variations or pulses in the strength of the nocturnal jet were also observed in the wind speed data both at the gap and by the lidar (Figs. 12, 5, and 8). The most obvious long period of variation is the reduction in down-basin flow between ~0900 and 1200 UTC during IOP 5, noted in sections 3a and 3b (Figs. 5 and 8). This weakening of the southerly flow appears strongly in the sodar data. The timing is nearly simultaneous with that seen in the lidar data, reinforcing the idea that this was a larger-scale, or at least basin-scale, effect.

Fluctuations of the flow strength at the NCAR site, which were observed almost every night and which were most evident in the 10-m wind speeds (Fig. 12), had periods ranging from 1 to 6 h and amplitudes of up to 6 m s^{-1}. Pulses with higher- and lower-frequency characteristics can be identified. The higher-frequency (1–2 h) pulses of ~2 m s^{-1} peak-to-peak amplitude can be seen most strongly in the 10-m data during IOPs 4, 5, 6, and 8, and in the sodar data (averaged over the height interval from 50 to 100 m) during IOPs 6 and 8. The amplitudes of these pulses diminished with height: they were reduced at the hill site (not shown) and appeared smaller still in the sodar winds. The longer-period, larger-amplitude pulses in the anemometer trace (Fig. 12) penetrated deeper into the boundary layer. They still appear strong in the sodar winds aloft, and the pulses detected by the sodar were generally correlated with the pulses near the surface. A singular jump of ~5 m s^{-1} at 1045 UTC during IOP 7 also diminished rapidly with height. We note that only the longer period of variations (3.5–8 h) are evident midbasin in the Doppler lidar data (Fig. 8). Thus, the smaller-amplitude, higher-frequency pulses were shallow and seemed to be of little consequence, but the larger-amplitude pulses extended through the lowest few hundred meters and may have promoted vertical transport through the surface-based stable layer. The effects of these pulsing events on vertical mixing and the influence of the nocturnal jet on boundary layer stability in the gap are addressed further in Pinto et al. (2004, manuscript submitted to *Mon. Wea. Rev.*).

Thus, the flow through the gap was a part of the southerly flow from the Utah Lake basin through the GSL basin and an important factor in interbasin transport and exchange of air masses. The gap produces a constriction and partial blocking of the stable flow. The flow through the constriction and over the ridge at the gap produced waves and pulses that were seen in the observations at Jordan Narrows (see also Fig. 8 of Doran et al. 2002). Such pulsing and wave events often produce local regions of convergence and w, as illustrated in Fig. 2. As the flow then expanded into the GSL basin, the jet wind speeds diminished slightly.

g. Discussion: Impact of basin-scale jet

The existence of a moderately strong down-basin flow in the GSL basin instead of the weak, locally generated flows expected in a simple basin affected the processes listed in section 2. These effects included the following:

- Canyon outflows were present but their penetration into the basin and their organization could be significantly reduced by strong southerly flow in the basin.
- Basinwide processes (radiative cooling, shear-generated mixing at the cold-pool inversion) were still active, but in a modified form because of the shear generated by the jet.
- Downslope cold-air drainage flows were found to exist by an array of tethersondes along a slope in the basin; however, a significant down-basin (cross slope) wind component was superimposed.
- Basin-jet interactions with terrain-forced and with other flows produced significant but complex horizontal transport patterns within the basin cold pool.

Small-scale mixing and transport mechanisms that are important under stable conditions (e.g., Fig. 2) can be modified by a basin-scale jet in different ways.

- Some mechanisms are enhanced by stronger flows, such as obstacle effects and waves (e.g., those noted downstream of Jordan Narrows), whereas
- other mechanisms are reduced in importance (e.g., those related to surface cooling and drainage effects).

In addition to modifying mechanisms, the basin jet also produces new ones. For example,

- LLJs produce a layer of enhanced shear between the

jet maximum and the surface, which can generate turbulence and mixing below the jet as found for the nocturnal LLJ over the Great Plains (Banta et al. 2002, 2003; Mahrt and Vickers 2002). Evidence of this effect was found in the behavior of the temperature profiles below 75 m AGL.
- Convergence patterns focused between the canyon outflows and the LLJ (Figs. 7 and 10) are also examples, which were documented and explored numerically. The model showed a persistent $\gtrsim 5$ cm s^{-1} updraft associated with the convergence line,

Thus, the existence of a LLJ in the basin can give rise to vertical transport mechanisms that would not be present in a simple basin, and can alter others that would.

Cold-pool budget studies would also be significantly affected by the basin-scale jet. Small differences between inflow speeds into the basin from the south and outflows toward the GSL to the north should produce significant divergence (positive or negative) of mass, which could dominate all of the budgets. These effects are being studied using Doppler lidar scan data to estimate basinwide divergence and mean w over the basin. The purpose of these studies is to determine whether the basinwide divergence is large enough to significantly alter the budgets.

An important aspect of this study requiring further attention is that the down-basin jet was fully formed as it passed through the Jordan Narrows gap, and, thus, as described earlier, it was a feature of the basin complex, rather than just the GSL basin alone. Studying and fully understanding the origin of the jet and the total thermal forcing that produces it will require concurrent measurements in the Utah Lake basin and perhaps some of its major tributaries, as well as the mountains surrounding that basin.

4. Conclusions

A nocturnal low-level jet blowing down the basin was discovered by Doppler lidar scan data in the Great Salt Lake basin under weak synoptic forcing. On such nights this jet was a dominant feature of the flow in the basin. Such a jet has not been noted in other studies in simple basins. The linking together of the GSL basin with other basins to the south via the Jordan Narrows gap was found to alter the behavior of the flow along the basin axis, making it more similar to a flow in a long channel or valley.

Here we have used the monthlong VTMX dataset to identify several nights with thermally forced jets within the basin. We have shown that the jet occurred on many different nights and that its development differed from night to night, depending on the strength of the large-scale low-level pressure gradient. We have also shown how such differences in the properties and timing of the jet produce differences in other aspects of the flow in the basin, such as convergence/vertical motion regions.

One of the reasons for going into the field for a month is to obtain a variety of cases. Each case is different. As features of the flow are discovered, it is important to determine whether they only occur under very specific conditions external to the basin, (i.e., did they only occur on the one day when they were first found?), or whether a wide range of conditions can produce these features. This is especially important for numerical weather prediction (NWP) modeling applications, because it is necessary to evaluate a model by knowing not only 1) whether it is capable of producing (under carefully controlled model conditions) features that resemble features that were observed, but, especially, 2) to determine whether the model is similar to the atmosphere in its *response* to *changes* in external conditions. The latter is more important to a complete evaluation of the model's capabilities as well as to a complete understanding of the phenomenon being studied.

It is a relatively straightforward exercise to perform sensitivity tests with a numerical model. Determining the response of atmospheric flow features to external changes is much more difficult, because it must come from measurement campaigns that are comprehensive enough to document all quantities relevant to the investigation, and over a long enough period to include at least several occurrences of the phenomenon of interest. Unfortunately, such datasets are expensive and difficult to obtain, so not many exist. Obviously, a high priority should be to include such atmospheric ''sensitivity studies'' into experimental design. Another priority should be to analyze those cases that do exist to reveal the sensitivity of important atmospheric features to changing external conditions. These analyses, in turn, can be used in NWP modeling studies to see whether the features simulated by the model exhibit similar sensitivity, that is, to assess whether the models properly mimic the response of the atmosphere to external changes.

The most important factor in transport and dispersion of atmospheric contaminants is getting the advecting wind field right. This is challenging in a basin or other complex terrain setting. It becomes *especially* challenging, however, under stable conditions, where overall mixing levels are suppressed, and flow features of a small scale persist and perform most of the transport and mixing. In the present study the dependence of the basin jet on the larger-scale pressure gradient and the controlling influence of the jet on other smaller-scale flows in the basin are key elements of the within-basin wind field. Because of the dominant role of the jet in atmospheric transport within the basin, being able to characterize and model it, as well as its effect on other flows, is essential for many applications. Air quality and emergency response, for example, are significantly affected by this transport and by the resulting distributions and concentrations of atmospheric contaminants or pollutants. Accurate representation of these flows is thus

critical for such applications, which involve the health and lives of people.

Acknowledgments. This work was supported by the U.S. Department of Energy, under the auspices of the Environmental Meteorology Program of the Office of Biological and Environmental Research, through Interagency Agreement DE-AI03-99ER62842. We appreciate the support of project managers Rickey C. Petty and Peter Lunn, and we also appreciate the efforts of the following individuals, who worked during the field campaign to ensure the success of the lidar measurement effort: Raul Alvarez, Alan Brewer, Sherlyn Cooley, Janet Intrieri, Brandi McCarty, Richard Marchbanks, Scott Sandberg, and Joe Shaw. We thank Yelena Pichugina for her aid in manuscript preparation, and we thank Andreas Muschinski and Robert Zamora for helpful reviews of the manuscript.

REFERENCES

Allwine, K. J., B. K. Lamb, and R. Eskridge, 1992: Wintertime dispersion in a mountainous basin at Roanoke, Virginia: Tracer study. *J. Appl. Meteor.,* **31,** 1295–1311.

——, J. H. Shinn, G. E. Streit, K. L. Clawson, and M. Brown, 2002: Overview of URBAN 2000: A multiscale field study of dispersion through an urban environment. *Bull. Amer. Meteor. Soc.,* **83,** 521–536.

Atkinson, B. W., 1981: *Mesoscale Atmospheric Circulations.* Academic Press, 279 pp.

Banta, R. M., 1984: Daytime boundary-layer evolution over mountainous terrain. Part I: Observations of the dry circulations. *Mon. Wea. Rev.,* **112,** 340–356.

——, 1985: Late-morning jump in TKE in the mixed layer over a mountain basin. *J. Atmos. Sci.,* **42,** 407–411.

——, 1986: Daytime boundary-layer evolution over mountainous terrain. Part II: Numerical studies of upslope flow duration. *Mon. Wea. Rev.,* **114,** 1112–1130.

——, and W. R. Cotton, 1981: An analysis of the structure of local wind systems in a broad mountain basin. *J. Appl. Meteor.,* **20,** 1255–1266.

——, L. D. Olivier, W. D. Neff, D. H. Levinson, and D. Ruffieux, 1995: Influence of canyon-induced flows on flow and dispersion over adjacent plains. *Theor. Appl. Climatol.,* **52,** 27–42.

——, ——, P. H. Gudiksen, and R. Lange, 1996: Implications of small-scale flow features to modeling dispersion over complex terrain. *J. Appl. Meteor.,* **35,** 330–342.

——, and Coauthors, 1997: Nocturnal cleansing flows in a tributary valley. *Atmos. Environ.,* **31,** 2147–2162.

——, L. S. Darby, P. Kaufmann, D. H. Levinson, and C.-J. Zhu, 1999: Wind flow patterns in the Grand Canyon as revealed by Doppler lidar. *J. Appl. Meteor.,* **38,** 1069–1083.

——, R. K. Newsom, J. K. Lundquist, Y. L. Pichugina, R. L. Coulter, and L. Mahrt, 2002: Nocturnal low-level jet characteristics over Kansas during CASES-99. *Bound.-Layer Meteor.,* **105,** 221–252.

——, Y. L. Pichugina, and R. K. Newsom, 2003: Relationship between low-level jet properties and turbulence kinetic energy in the nocturnal stable boundary layer. *J. Atmos. Sci.,* **60,** 2549–2555.

Barr, S., and M. M. Orgill, 1989: Influence of external meteorology on nocturnal valley drainage winds. *J. Appl. Meteor.,* **28,** 497–517.

Barry, R. G., 1992: *Mountain Weather and Climate.* 2d ed. Routledge, 402 pp.

Chen, C., and W. R. Cotton, 1983: A one-dimensional simulation of the stratocumulus-capped mixed layer. *Bound.-Layer Meteor.,* **25,** 289–321.

Clements, C. B., C. D. Whiteman, and J. D. Horel, 2003: Cold air pool structure and evolution in a mountain basin: Peter Sinks, Utah. *J. Appl. Meteor.,* **42,** 752–768.

Clements, W. E., J. A. Archuleta, and D. E. Hoard, 1989: Mean structure of the nocturnal drainage flow in a deep valley. *J. Appl. Meteor.,* **28,** 457–462.

Cornman, L. B., R. K. Goodrich, C. S. Morse, and W. L. Ecklund 1998: A fuzzy logic method for improved moment estimation from Doppler spectra. *J. Atmos. Oceanic Technol.,* **15,** 1287–1305.

Coulter, R. L., and P. Gudiksen, 1995: The dependence of canyon winds on surface cooling and external forcing in Colorado's Front Range. *J. Appl. Meteor.,* **34,** 1419–1429.

Darby, L. S., W. D. Neff, and R. M. Banta, 1999: Multiscale analysis of a meso-β frontal passage in the complex terrain of the Colorado Front Range. *Mon. Wea. Rev.,* **127,** 2062–2081.

Davidson, B., and P. K. Rao, 1963: Experimental studies of the valley-plain wind. *Int. J. Air Water Pollut.,* **7,** 907–923.

Doran, J. C., 1991: The effects of ambient winds on valley drainage flows. *Bound.-Layer Meteor.,* **55,** 177–189.

——, 1996: The influence of canyon winds on flow fields near Colorado's Front Range. *J. Appl. Meteor.,* **35,** 587–600.

——, J. D. Fast, and J. Horel, 2002: The VTMX 2000 Campaign. *Bull. Amer. Meteor. Soc.,* **83,** 537–551.

Fast, J. D., and L. S. Darby, 2004: An evaluation of mesoscale model predictions of down-valley and canyon flows and their consequences using Doppler lidar measurements. *J. Appl. Meteor.,* **43,** 420–436.

——, S. Zhong, and C. D. Whiteman, 1996: Boundary layer evolution within a Canyonland basin. Part II: Numerical simulations of nocturnal flows and heat budgets. *J. Appl. Meteor.,* **35,** 2162–2178.

——, L. S. Darby, and R. M. Banta, 2002: The interaction of down-valley and canyon flows and their effect on mean vertical motions in the Salt Lake Valley. Preprints, *10th Conf. on Mountain Meteorology,* Park City, UT, Amer. Meteor. Soc., 2–5.

Geiger, R., 1965: *The Climate Near the Ground.* Review ed. Harvard University Press, 611 pp. [Translated by Scripta Technica, Inc., from the German 4th ed., 1961.]

Gudiksen, P. H., J. M. Leone, C. W. King, D. Ruffieux, and W. D. Neff, 1992: Measurements and modeling of the effects of ambient meteorology on nocturnal drainage flows. *J. Appl. Meteor.,* **31,** 1023–1032.

Hawkes, H. B., 1947: Mountain and valley winds with special reference to the diurnal mountain winds of the Great Salt Lake region. Ph.D. dissertation, Ohio State University, 312 pp.

Helfand, H. M., and J. C. Labraga, 1988: Design of a nonsingular level 2.5 second-order closure model for the prediction of atmospheric turbulence. *J. Atmos. Sci.,* **45,** 113–132.

Holland, L. D., 2002: Downslope windstorms along the Wasatch Front. M. S. thesis, University of Utah, 86 pp.

Horel, J., and Coauthors, 2002: MesoWest: Cooperative mesonets in the western United States. *Bull. Amer. Meteor. Soc.,* **83,** 211–226.

Kao, S. K., H. N. Lee, and K. I. Smidy, 1975: An analysis of the topographical effect on turbulence and diffusion in the atmosphere's boundary layer. *Bound.-Layer Meteor.,* **8,** 323–334.

Kelly, R. D., 1988: Asymmetric removal of temperature inversions in a high mountain valley. *J. Appl. Meteor.,* **27,** 664–673.

King, C. W., 1997: A climatology of thermally forced circulations in oppositely oriented airsheds along the Continental Divide in Colorado. Ph.D. dissertation, University of Colorado, and NOAA Tech. Memo. ERL-ETL-283, 132 pp.

Levinson, D. H., and R. M. Banta, 1995: Observations of a terrain-forced mesoscale vortex and canyon drainage flows along the Front Range of the Colorado Rockies. *Mon. Wea. Rev.,* **123,** 2029–2050.

Mahrt, L., and D. Vickers, 2002: Contrasting vertical structures of

nocturnal boundary layers. *Bound.-Layer Meteor.*, **105,** 351–363.
Mellor, G. L., and T. Yamada, 1982: Development of a turbulence closure model for geophysical fluid problems. *Rev. Geophys. Space Phys.*, **20,** 851–875.
Morse, C. S., R. K. Goodrich, and L. B. Cornman 2002: The NIMA method for improved moment estimation from Doppler spectra. *J. Atmos. Oceanic Technol.*, **19,** 274–295.
Neff, W. D., 1990: Remote sensing of atmospheric processes over complex terrain. *Atmospheric Processes over Complex Terrain, Meteor. Monogr.*, No. 23, Amer. Meteor. Soc., 173–228.
——, and C. W. King, 1989: The accumulation and pooling of drainage flows in a large basin. *J. Appl. Meteor.*, **28,** 518–529.
Nickus, U., and I. Vergeiner, 1984: The thermal structure of the Inn Valley atmosphere. *Arch. Meteor. Geophys. Bioclimatol. Ser. A*, **33,** 199–215.
Olivier, L. D., and G. S. Poulos, 1998: Frontal passage, mountain waves and flow reversals in the vicinity of the Colorado Springs, CO Airport. Preprints, *Eighth Conf. on Mountain Meteorology*, Flagstaff, AZ, Amer. Meteor. Soc., 176–181.
Petkovšek, Z., 1978: Relief meteorologically relevant characteristics of basins. *Z. Meteor.*, **28,** 333–340.
——, 1980: Additional relief meteorologically relevant characteristics of basins. *Z. Meteor.*, **30,** 379–382.
Pielke, R. A., and Coauthors, 1992: A comprehensive meteorological modeling system—RAMS. *Meteor. Atmos. Phys.*, **49,** 69–91.
Post, M. J., and W. D. Neff, 1986: Doppler lidar measurements of winds in a narrow mountain valley. *Bull. Amer. Meteor. Soc.*, **67,** 274–281.
——, and R. E. Cupp, 1990: Optimizing a pulsed Doppler lidar. *Appl. Opt.*, **29,** 4145–4158.
Sassen, K., 1994: Advances in polarization diversity lidar for cloud remote sensing. *Proc. IEEE*, **82,** 1907–1914.
Shaw, W. J., L. S. Darby, and R. M. Banta, 2003: A comparison of winds measured by a 915 MHz wind profiling radar and a Doppler lidar. Preprints, *12th Symp. on Meteorological Observations and Instrumentation*, Long Beach, CA, Amer. Meteor. Soc., P1.8.
Steinacker, R., 1988: On the value and evaluation of pressure information in mountain areas. Vol. II, ICAM/CIMA, Servizio Meteorologico Italiano, 7 pp.
Sterten, A. K., and J. Knudsen, 1961: Local and synoptic meteorological investigations of the mountain and valley wind system. Forsvarets Forskningsinstitutt, Norwegian Defence Research Establishment, Intern Rapport K-242, 139 pp.
Tyson, P. D., and R. A. Presont-Whyte, 1972: Observations of regional topographically-induced wind systems in Natal. *J. Appl. Meteor.*, **11,** 643–650.
Vergeiner, I., and E. Dreiseitl, 1987: Valley winds and slope winds-observations and elementary thoughts. *Meteor. Atmos. Phys.*, **36,** 264–286.
Weissmann, M. D., G. J. Mayr, R. M. Banta, and A. Gohm, 2004: Observations of the temporal evolution and spatial structure of gap flow in the Wipp Valley on 2 and 3 October 1999. *Mon. Wea. Rev.*, **132,** 2684–2697.
Whiteman, C. D., 1982: Breakup of temperature inversions in deep mountain valleys: Part I. Observations. *J. Appl. Meteor.*, **21,** 270–289.
——, 1990: Observations of thermally developed wind systems in mountainous terrain. *Atmospheric Processes over Complex Terrain, Meteor. Monogr.*, No. 23, Amer. Meteor. Soc., 5–42.
——, and K. J. Allwine, 1986: Extraterrestrial solar radiation on inclined surfaces. *Environ. Software*, **1,** 164–169.
——, and J. C. Doran, 1993: The relationship between overlying synoptic-scale flows and winds within a valley. *J. Appl. Meteor.*, **32,** 1669–1682.
——, T. B. McKee, and J. C. Doran, 1996: Boundary layer evolution within a Canyonland basin. Part I: Mass, heat, and moisture budgets from observations. *J. Appl. Meteor.*, **35,** 2145–2161.
——, S. Zhong, and X. Bian, 1999: Wintertime boundary-layer structure in the Grand Canyon. *J. Appl. Meteor.*, **38,** 1084–1102.
Zhong, S., and J. D. Fast, 2003: An evaluation of the MM5, RAMS, and Meso-Eta models at subkilometer resolution using field campaign data in the Salt Lake Valley. *Mon. Wea. Rev.*, **131,** 1301–1322.